

Mining self-similarity: Label super-resolution with epitomic representations

Nikolay Malkin¹, Anthony Ortiz², and Nebojsa Jojic³

¹ Yale University, New Haven, CT 06520, USA
kolya.malkin@yale.edu

² Microsoft AI for Good Research Lab, Redmond, WA 98052, USA

³ Microsoft Research, Redmond, WA 98052, USA
{anthony.ortiz,jojic}@microsoft.com

Abstract. We show that simple patch-based models, such as epitomes (Jojic et al., 2003), can have superior performance to the current state of the art in semantic segmentation and label super-resolution, which uses deep convolutional neural networks. We derive a new training algorithm for epitomes which allows, for the first time, learning from very large data sets and derive a label super-resolution algorithm as a statistical inference over epitomic representations. We illustrate our methods on land cover mapping and medical image analysis tasks.

Keywords: Label super-resolution, Semantic segmentation, Self-similarity

1 Introduction

Deep convolutional neural networks (CNNs) have become a tool of choice in computer vision. They typically outperform other approaches in core tasks such as object recognition and segmentation, but suffer from several drawbacks. First, CNNs are hard to interpret, which makes them difficult to improve by adding common-sense priors or invariances into the architecture. Second, they are usually trained in a supervised fashion on large amounts of labeled data, yet in most applications labels are sparse, leading to various domain adaptation challenges. Third, there is evidence of failure of the architecture choices that were meant to promote CNNs' reasoning over large distances in images. The *effective* receptive field [24] of CNNs – the distance at which faraway pixels stop contributing to the activity of deeper neurons – is often a small fraction of the theoretical one.

With the third point in mind, we ask a simple question, the answer to which can inform an agenda in building models which are interpretable, can be pre-trained in an unsupervised manner, adopt priors with ease, and are amenable to well-understood statistical inference techniques: *If deep CNNs effectively use only small image patches for vision tasks, and learn from billions of pixels, then how would simple exemplar-like approaches perform, and can they be made practical computationally?* We show that models based on epitomic representations [20], illustrated in Fig. 2, match and surpass deep CNNs on several weakly supervised segmentation and domain transfer tasks.

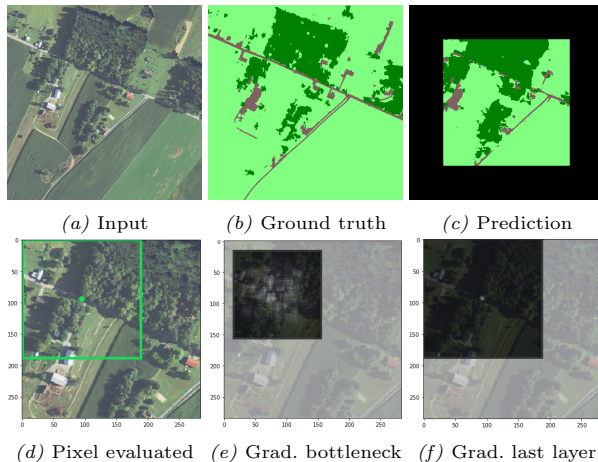


Fig. 1. Gradient-based effective receptive field estimation: We use the gradients from selected intermediate layers to the input image to estimate the size of the effective receptive field. In (e), we visualize the normalized gradient map (at a single coordinate shown on green in (d)) of the U-Net’s bottleneck (highest downsampling) layer with respect to the input image; (f) shows gradients of the *final* layer for the same pixel. The dark squares show the theoretical receptive field of the layers in question (139×139 for the bottleneck and 183×183 for the final layer). However, the gradient map (f) suggests that the effective receptive field is only about 13×13 pixels on average

For example, in Fig. 1 we show a patch of aerial imagery and the output of a U-Net [37] trained to predict land cover. The network misclassifies as vegetation the road pixels that appear in tree shadows. The model was trained on a large land cover map [8,35] that presents many opportunities to learn that roads are long and uninterrupted. The land cover data contains many more patterns that would help see rivers through a forest, recognize houses based on their proximity to roads, etc., but the U-Nets do not seem to learn such long-range patterns. This myopic behavior has been observed in other architectures as well [24,7,14].

In contrast, our algorithms directly model small image patches, forgoing long-range relationships. As generative models of images, epitomes are highly interpretable: they look like the images they were trained on (Fig. 2). Our generative formulation of image segmentation allows the inference of labels in the latent variable space, with or without high-resolution supervision (Fig. 4). They achieve comparable performance to the state-of-the-art CNNs on semantic segmentation tasks, and surpass the CNNs’ performance in domain transfer and weakly supervised (label super-resolution) settings.

In summary, our contributions are as follows:

(1) As previous training algorithms fail to fit large epitomes well, we develop new algorithms that are suitable for mining self-similarity in very large datasets.

(2) We develop a new label super-resolution formulation that mines image self-similarity using epitomes or directly in a single (small) image.

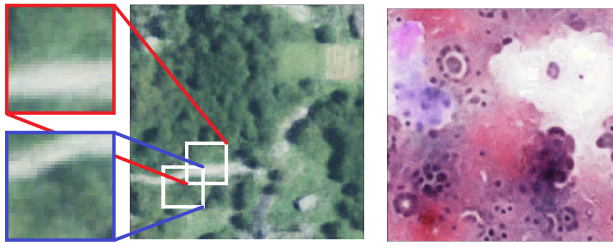


Fig. 2. A quarter of an epitome (μ parameters shown) trained on aerial imagery (*left*) and an epitome trained on pathology slides (*right*). Any 31×31 training data patch is generated by, and likely similar to, some 31×31 window in the epitome. Note the two overlapping windows: the patches are distant in color space, but their corresponding mixture components share parameters on the intersection. The epitomes are $200\times$ and $30000\times$ smaller, respectively, than their total training data

(3) We show how these models surpass the recent (neural network) state of the art in aerial and pathology image analysis.

(4) We illustrate that our approaches allow and even benefit from unsupervised pre-training (separation of feature learning from label embedding).

(5) We show that our models deal with data size gracefully: We can train an epitome on a large fully labeled aerial imagery / land cover map and obtain better transfer in a new geography than CNNs [25,35], but we get even better results by analyzing one 512×512 tile at a time, with only low-resolution labels.

2 Epitomes as segmentation models

Epitomes [20] are an upgraded version of a Gaussian mixture model of image patches. In this section we present, for completeness, the definition of these models. We then explain how they can be turned into segmentation models.

Consider a training set consisting of image patches x^t unwrapped as vectors $x^t = \{x_{i,j,k}^t\}$, where i, j are coordinates in the patch and k is the spectral channel (R,G,B,...), and the corresponding vector of one-hot label embeddings $y_t = \{y_{i,j,\ell}^t\}$, $\ell \in \{1, \dots, L\}$. In a mixture model, the distribution over the (image, label) data is represented with the aid of a latent variable $s \in \{1, \dots, S\}$ as

$$p(x^t, y^t) = \sum_{s=1}^S p(x^t|s)p(y^t|s)p(s), \quad (1)$$

where $p(s)$ is the frequency of a mixture component s , while the conditional probability $p(x^t|s)$ describes the allowed variation in the image patch that s generates and $p(y^t|s)$ describes the likely labels for it. Under this model, the estimate for \hat{y} , the expected segmentation of a new image x , is

$$p(y|x) = \sum_s p(s|x)p(y|s). \quad (2)$$

A natural choice for $p(x|s)$ is a diagonal Gaussian distribution,

$$p(x|s) = \prod_{i,j,k} \frac{\exp\left(-\frac{1}{2}(x_{i,j,k} - \mu_{s,i,j,k})^2/\sigma_{s,i,j,k}^2\right)}{(2\pi\sigma_{s,i,j,k}^2)^{\frac{1}{2}}} \quad (3)$$

and for $p(y|s)$ a product of categorical distributions over labels at each pixel position. The mean of the mixture component s contains pixel values $\mu_{s,i,j,k}$, while the covariance matrix is expressed in terms of its diagonal elements $\sigma_{s,i,j,k}^2$, the variances of different color channels k for individual pixels i, j .

Epitomic representations [20] compress this parametrization by recognizing that patches of interest come from *overlapping* regions and that different components s should share parameters. The component index $s = (s_1, s_2)$ lives on a $N \times N$ grid, so $0 \leq s_1, s_2 \leq N - 1$, and the parameters are shared:

$$\mu_{s,i,j,k} = \boldsymbol{\mu}_{s_1+i, s_2+j, k} \quad \sigma_{s,i,j,k}^2 = \boldsymbol{\sigma}_{s_1+i, s_2+j, k}^2 \quad (4)$$

(Indices are to be interpreted modulo N , i.e., with toroidal wrap-around.) Thus, the epitome is a large grid of parameters $\boldsymbol{\mu}_{m,n,k}, \boldsymbol{\sigma}_{m,n,k}$, so that the parameters for the mixture component $s = (s_1, s_2)$ start at position s_1, s_2 and extend to the left and down by the size of the patch, as shown in Fig. 2. Modeling $K \times K$ patches will take K^2 times fewer parameters for the similar expressiveness as a regular mixture model trained on $K \times K$ patches. The posterior $p(s|x) \propto p(x|s)p(s)$ is efficiently computed using convolutions/correlations, e.g.,

$$p(s_1, s_2|x) \propto \exp \sum_{i,j,k} \frac{-1}{2} \left(\frac{x_{i,j,k}^2}{\boldsymbol{\sigma}_{s_1+i, s_2+j, k}^2} - \frac{2x_{i,j,k}\boldsymbol{\mu}_{s_1+i, s_2+j, k}}{\boldsymbol{\sigma}_{s_1+i, s_2+j, k}^2} + \frac{\boldsymbol{\mu}_{s_1+i, s_2+j, k}^2}{\boldsymbol{\sigma}_{s_1+i, s_2+j, k}^2} + \log \boldsymbol{\sigma}_{s_1+i, s_2+j, k}^2 \right) \cdot p(s_1, s_2). \quad (5)$$

Epitomes are a summary of self-similarity in the images on which they are trained. They should thus contain a much smaller number of pixels than the training imagery, but be much larger than the patches with which they are trained. Each pixel in the epitome is contained in K^2 patches of size $K \times K$ and can be tracked back to many different positions in many images.

Conversely, this mapping of images enables embedding of *labels* into the epitome after the epitome of the images x has been trained. Every location in the epitome m, n will have (soft) label indicators $z_{m,n,\ell}$, computed as

$$p(\ell|m, n) \propto z_{m,n,\ell} = \sum_t \sum_{s_1, s_2: (m,n) \in W_{s_1, s_2}} p(s_1, s_2|x^t) y_{m-s_1, n-s_2, \ell}^t, \quad (6)$$

where W_{s_1, s_2} is the epitome window starting at (s_1, s_2) , i.e. the set of K^2 coordinates (m, n) in the epitome that belong to the mixture component (s_1, s_2) . The posterior tells us the strength of the mapping of the patch x^t to each component s that overlaps the position (m, n) . The corresponding location in the patch of labels y^t is $(m - s_1, n - s_2)$, so $y_{m-s_1, n-s_2, \ell}^t$ is added to the count $z_{m,n,\ell}$ of label ℓ at location (m, n) . Finally, we declare $p(y_{i,j,\ell}|s_1, s_2) \propto z_{s_1+i, s_2+j, \ell}$, allowing inference of ℓ for a new image patch by (2).



Fig. 3. Numerical near-fixed points of naïve epitome training by SGD without location promotion, caused by vanishing posteriors, and a 399×399 epitome trained with location promotion (*left*); non-diversifying and self-diversifying 499×499 epitomes trained on imagery of forests (*right*)

3 A large-scale epitome training algorithm

Epitomes have been used in recognition and segmentation tasks, e.g. [38,28,6,27,30,44,31,45]. However, the standard EM training algorithm [20] that maximizes the data log-likelihood $\sum_t \log \sum_s p(x^t|s)p(s)$ is not suitable to building *large* epitomes of *large* data sets due to the problem of “vanishing posterior”. As training advances, the dynamic range of the posterior $p(s|x^t)$ becomes too big for machine precision, and the small probabilities are set to zero. Further parameter updates discourage mapping to these unlikely positions, leading to a die-off of chunks of “real estate” in the epitome. The problem is exacerbated by the size of the data (and of the epitome). Due to stability issues or computational cost, previous solutions to this [21] do not allow the models to be trained on the scale on which neural networks are trained. The analogous problem exists in estimating the prior $p(s)$ over epitome positions, which also needs to have a large dynamic range. If the range is flatter (e.g., if we use a uniform prior) then maximization of likelihood requires that the epitome learn only the most frequent patterns in the data, replicating slight variations of them everywhere. As imagery is mostly uniform and smooth, this creates blurry epitomes devoid of rarer features with higher variances, like various edges and corners.

Instead of EM, we develop a large-scale epitome learning algorithm combining three important ingredients: stochastic gradient descent, location promotion techniques, and the diversity-promoting optimization criterion:

Stochastic gradient descent. Instead of changing the parameters of the model based on all data at once, we update them incrementally in the direction of the gradient of the log-likelihood of a batch of individual data points $\frac{d}{d\theta} \log \sum_t \sum_s p(x^t|s)p(s)$, where $\theta = \{\mu_{m,n,k}, \sigma_{m,n,k}^2, p(s_1, s_2)\}$. Note that gradient descent alone does not solve the vanishing posterior problem, as the posterior also factors into the expression for the gradient (see the SI). In fact, SGD makes the situation worse (Fig. 3): the model parameters evolve before all of the data is seen, thus speeding up the extinction of the epitome’s “real estate”.

Location promotion. To maintain the relatively uniform evolution of all parts of the epitome, we directly constrain the learning procedure to hit all areas of the epitome through a form of posterior regularization [13]. Within an SGD framework, this can be accomplished simply by keeping counters R_{s_1, s_2} at each

position s_1, s_2 and incrementing them by the posterior $p(s_1, s_2|x^t)$ upon every sample x^t , then disallowing mapping to the windows s_1, s_2 which contain the *most frequently* mapped pixels. In particular, we compute a mask $M = \{R_{s_1, s_2} < c/N^2\}$, where $N \times N$ is the size of the epitome, for some small constant $c < 1$, and optimize only $\log \sum_{(s_1, s_2) \in M} p(x^t|s_1, s_2)p(s_1, s_2)$ at each gradient descent step. When $|M| > (1 - \delta)|N|^2$ for some small δ , all counters are reset to 0.

Diversification training. As illustrated in Fig. 3 (right), standard SGD tends to learn uniform patterns, especially when trained on large datasets. Just like EM, it has to rely on the prior $p(s)$ to avoid learning blurry epitomes, but the dynamic range needed to control this is too high. Additionally, through location promotion, we in fact encourage more uniform coverage of locations. Thus, we change the optimization criterion from log-likelihood of *all* data to log-likelihood of the worst modeled subset of each batch, $\sum_{t \in L_p} \sum_s p(x^t|s)$, where L_p is the set of data in the worst-modeled quantile p (the lowest quarter, in our experiments) in terms of data likelihood, either under a previously trained model or under the model being trained (*self-diversification*). This version of a max-min criterion avoids focusing on outliers while ensuring that the data is uniformly well modeled. The resulting epitomes capture a greater variety of features, as seen in the right panel of Fig. 3. The diversification criterion also helps the model generalize better on the test set, as we show in the experiments.

In the SI, we provide the details of the training parameters and analysis of execution time. The simple and runnable example training code⁴ illustrates all three features of the algorithm.

4 Label super-resolution by self-similarity

Labeling images at a pixel level is costly and time-consuming, so a number of semi-supervised approaches to segmentation have been studied, e.g., [29,10,17,33]. Recently, [25] proposed a “label super-resolution” (LSR) technique which uses statistics of occurrence of high-resolution labels within coarse blocks of pixels labeled with a different set of low-resolution classes. (For clarity, we refer to low-res information as *classes* and high-res information as *labels*.) Each class, indexed by c , has a different composition of high-resolution labels, indexed by ℓ .

The label super-resolution technique in [25] assumes prior knowledge of the compositions $p(\ell|c)$ of high-res labels in low-res classes and uses them to define an alternative optimization cost at the top of a core segmentation network that predicts the high-res labels. Training the network end-to-end with coarse classes results in a model capable of directly predicting the high-res labels of the individual pixels. Backpropagation through such alternative cost criteria is prone to collapse, and [25] reports best results when the data with high-res labels (HR) is mixed with data with low-res labels (LR). Furthermore, the problem is inherently ill-posed: given an expressive enough model and a perfect learning algorithm, many solutions are possible. For example, the model could learn

⁴ https://github.com/anthonymlortiz/epitomes_lsr

to recognize an individual low-res block and then choose an arbitrary pattern of high-res labels within it that satisfies the counts $p(\ell|c)$. Thus the technique depends on the inductive biases of the learning algorithm and the network architecture to lead to the desirable solutions.

On the other hand, following statistical models we discuss here, we can develop a statistical LSR inference technique from first principles. The data x is modeled by a mixture indexed by the latent index s . Using this index to also model the structure in the joint distribution over labels ℓ inside the patches generated by component s and classes c to which the patches belong, the known distribution of labels given the classes should satisfy $p(\ell|c) = \sum_s p(\ell|s)p(s|c)$. Thus, we find the label embedding $p(\ell|s)$ by minimizing the KL distance between the known $p(\ell|c)$ and the model’s prediction $\sum_s p(\ell|s)p(s|c)$, i.e, by solving

$$p(\ell|s) = \arg \max_{p(\ell|s)} \sum_c p(c) \sum_\ell p(\ell|c) \log \sum_s p(\ell|s)p(s|c), \quad (7)$$

where $p(c)$ are the observed proportions of low-res classes in the data and $p(s|c)$ is obtained as the posterior over s for data of label c , as we will discuss in a moment. First, we derive an EM algorithm for solving the problem in Eq. 7 using auxiliary distributions $q_{\ell,c}(s)$ to repeatedly bound $\log \sum_s p(\ell|s)p(s|c)$ and reestimate $p(\ell|s)$. To derive the E step, we observe that

$$\log \sum_s p(\ell|s)p(s|c) = \log \sum_s q_{\ell,c}(s) \frac{p(\ell|s)p(s|c)}{q_{\ell,c}(s)} \geq \sum_s q_{\ell,c}(s) \log \frac{p(\ell|s)p(s|c)}{q_{\ell,c}(s)}.$$

The bound holds for all distributions $q_{\ell,c}$ and is made tight for

$$q_{\ell,c}(s) \propto p(\ell|s)p(s|c). \quad (8)$$

Optimizing for $p(\ell|s)$, we get

$$p(\ell|s) \propto \sum_c p(c)p(\ell|c)q_{\ell,c}(s). \quad (9)$$

Coordinate ascent on the $q_{\ell,c}(s)$ and $p(\ell|s)$ by iterating (8) and (9) converges to a local maximum of the optimization criterion.

Therefore, all that is needed for label super-resolution are the distributions $p(s|c)$ that tell us how often each mixture component is seen within the class c . Given low-res labeled data, i.e., pairs (x^t, c^t) and a trained mixture model for image patches x^t , the answer is

$$p(s|c) \propto \sum_{t:c^t=c} p(s|x^t). \quad (10)$$

In other words, we go through all patches, look at the posterior of their assignment to prototypes s , and count how many times each prototype was associated with each of the classes.

The epitomic representation with its parameter sharing has an additional advantage here. With standard Gaussian mixtures of patches, the level of the

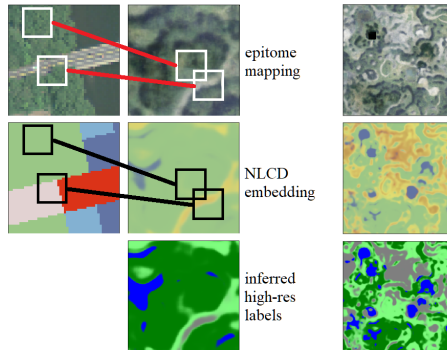


Fig. 4. Two image patches are shown mapped to a piece of an epitome (*left*). Below the source image, we show class labels for 30×30 m blocks. Below the epitome we show a piece of the class embedding $p(m, n|c)$ at a pixel level (Eqn. 11) using the same color scheme, with colors weighted by the inferred class probabilities. Below the class embedding we show the piece of the output of the label super-resolution algorithm in Section 4. We also show the full epitome and its embeddings (*right*)

super-resolution we can accomplish is defined by the size of the patch x we use in the analysis, because all of the reasoning is performed on the level of the patch index s , not at individual pixels. Thus, to get super-resolution at the level of a single pixel, our mixture model would have to be over individual pixels, i.e., a simple color clustering model (see the SI for examples). With epitomes, however, instead of using whole patch statistics, we can assign statistics $p(m, n|c)$ to individual positions in the epitome,

$$p(m, n|c) \propto \sum_t \sum_{i,j} p((s_1, s_2) = (m - i, n - j) | x^t) [c^t = c], \quad (11)$$

where $p(\cdot, \cdot | x^t)$ is the posterior over positions. This equation represents counting how many times each *pixel* in the epitome was mapped to by a patch that was inside a block of class c , as illustrated in Fig. 4: While the two patches map close to each other into the epitome, the all-forest patch is unlikely to cover any piece of the road. Considering all patches in a larger spatial context, the individual pixels in the epitome can get statistics that differ from their neighbors'. This allows the inference of high-res labels ℓ for the entire epitome, shown with its embedding of low-res classes c and super-resolved high-res labels ℓ on the right.

In summary, our LSR algorithm first uses the epitome model of $K \times K$ patches to embed class labels on an individual pixel level using Eq. 11. This then allows us to run the EM algorithm that iterates Eqs. 8 and 9 on positions m, n associated with the shared parameters in the epitome instead of mixture components s , using $p(m, n|c)$ in Eq. 11 in place of $p(s|c)$. Once the estimate of the high-res labels $p(\ell|m, n)$ is computed for each position in the epitome, we can predict labels in imagery using Eq. 2. This procedure performs probabilistic

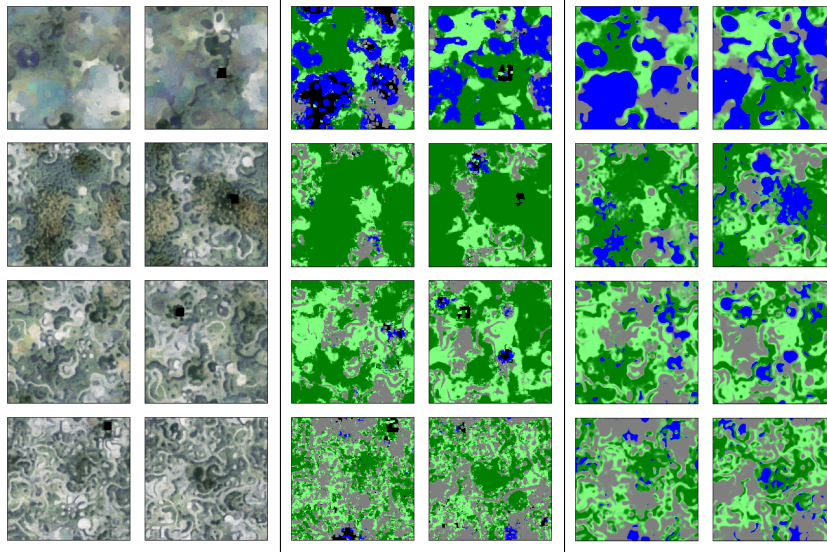


Fig. 5. Epitomes (total area $2 \cdot 10^6$ pixels) trained on $5 \cdot 10^9$ pixels of **South** imagery (*left*); land cover embeddings (argmax label shown) derived from high-resolution **South** ground truth (*middle*), land cover embeddings derived by epitomic LSR from **North** 30m-resolution NLCD data (*right*)

reasoning over the frequencies of repeating patterns in imagery labeled with low-resolution classes to reason over individual pixels in these patterns.

5 Experiments

5.1 Land cover segmentation and super-resolution

Our first example is the problem of land cover segmentation from aerial imagery. We work with the data studied by [35], available for $160,000\text{km}^2$ of land in the Chesapeake Bay watershed (Northeast US):

- (1) 1m-resolution 4-band aerial imagery (NAIP) taken in the years 2013-4;
- (2) High-resolution (1m) land cover segmentation in four classes (water, forest, field/low vegetation, built/impervious) produced by [8];
- (3) Low-resolution (30m) land cover labels from the National Land Cover Database (NLCD) [16].

As in [35], the data is split into **South** and **North** regions, comprising the states of MD, VA, WV, DE (S) and NY and PA (N). Our task is to produce 1m-resolution land cover maps of the **North** region, using only the imagery, possibly the low-res classes, and possibly the high-res labels from just the **South** region. The predictions are evaluated against high-res ground truth in the **North** region.

Despite the massive scale of the data, differences such as imaging conditions and frequency of occurrence of vegetation patterns make it difficult for neural

networks trained to predict high-res labels from imagery in the **South** region to transfer to **North**. However, in their study of this problem using data fusion methods, [35] obtained a large improvement in **North** performance by multi-task training: the networks were trained to predict high-res labels with the objectives of (1) cross-entropy loss against high-res labels in **South** and (2) super-resolution loss [25] against the distributions determined by low-res NLCD labels in **North** (see the first and third rows of Table 1).

Epitome training. We fit eight 499×499 epitomes to all available **South** imagery. To encourage a diversity of represented land types, for each of the four high-res labels ℓ (water, forest, field, built), we trained a self-diversifying epitome $E_0^{(\ell)}$ on patches of size 11×11 to 31×31 containing at least one pixel labeled with label ℓ . We then trained a model $E_1^{(\ell)}$ on the quarter of such patches with lowest likelihood under $E_0^{(\ell)}$ and a model $E_2^{(\ell)}$ on the quarter with lowest likelihood under $E_1^{(\ell)}$. The first epitome $E_0^{(\ell)}$ was then discarded.⁵ The final model is a uniform mixture of the $E_i^{(\ell)}$ ($i = 1, 2$). The $\mu_{m,n}$ parameters of its components can be seen in the left column of Fig. 5. (Notice that while the epitomes in each row were trained on patches containing pixels of a given label ℓ , other label appear in them as well. For example, we see roads in the forest epitome (second row), since roads are sometimes found next to trees, and indeed are poorly modeled by a model of only trees, cf. Fig. 3.)

High-resolution label embedding. We derive high-resolution soft label embeddings $p(\ell|m, n)$ from high-res **South** labels by the following procedure: for 10 million iterations, we uniformly sample a 31×31 patch of **South** imagery x^t and associated high-res labels y^t and evaluate the posterior over positions $p(s_1, s_2|x^t)$, then embed the center 11×11 patch of labels y^t weighted by the posterior (sped up by sampling; see the SI for details). The label embeddings $p(\ell|m, n) \propto z_{m,n,\ell}$ are proportional to the sum of these embeddings over all patches; these quantities estimate the probability that a patch generated by an epitome window with center near (s_1, s_2) would generate label ℓ at the corresponding position. These embeddings are shown in the middle column of Fig. 5.

Low-resolution NLCD embedding. Using the same set of epitomes trained on **South**, we derive the posteriors $p(m, n|c)$ given a low-resolution class c : we sample 11×11 patches x^t from **North** with center pixel labeled with low-res class c^t and embed the label c^t weighted by the posterior $p(s_1, s_2|x^t)$. By (11), $p(m, n|c)$ is then proportional to the sum of these embeddings. An example of the embeddings in one epitome component is shown in Fig. 4.

Epitomic label super-resolution. The joint distribution of high-res and low-res classes, $p(\ell|c)$, can be estimated on a small subset of jointly labeled data; we use the statistics reported by [25]. We apply our LSR algorithm to the low-res embeddings $p(m, n|c)$, the joint $p(c, \ell)$, and the known distribution $p(c)$ to arrive at high-res label probabilities at each epitome position, $p(\ell|m, n)$. They are shown in the right column of Fig. 5.

⁵ $E_2^{(\ell)}$ is trained to model the patches poorly modeled by the self-diversifying $E_1^{(\ell)}$. Hence, $E_2^{(\ell)}$ simply has much higher posteriors and more diversity of texture.

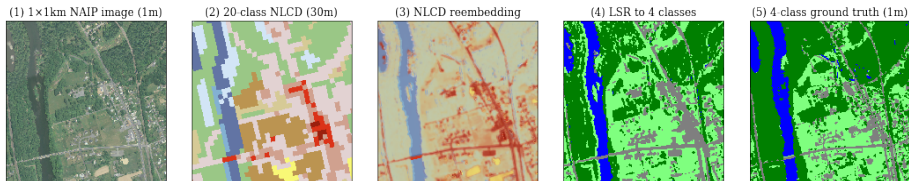


Fig. 6. Self-epitomic LSR on a 1024×1024 patch of land (1). The low-res classes (2) are embedded at locations similar in appearance, yielding (3). The inference procedure described in Sec. 4 produces (4), which closely resembles the ground truth (5)

Table 1. Performance of various methods on land cover segmentation in the **North** region. We report overall accuracy and mean intersection/union (Jaccard) index

Model	Label training set	Acc.	IoU
U-Net [35]	HR (S)	59.4%	40.5%
Epitome (S imagery)	HR (S)	79.5	59.3
U-Net neural LSR [25,35]	HR (S), LR (N)	86.9	62.5
U-Net neural LSR [25]	LR (N)	80.1	41.3
256^2 self-epitomic LSR	LR (N)	85.9	63.3
512^2 self-epitomic LSR	LR (N)	87.0	65.3
1024^2 self-epitomic LSR	LR (N)	87.8	66.9
2048^2 self-epitomic LSR	LR (N)	88.0	67.8
All-tile epitomic LSR	LR (N)	83.9	58.5

We evaluate the two epitome embeddings $p(\ell|m, n)$, derived from high-res labels in **South** or from low-res classes in **North**, on a sample of 1600km^2 of imagery in the **North** region in the following fashion: we select 31×31 patches x^t and reconstruct the labels in the center 11×11 blocks as the posterior-weighted mean of the $p(\ell|m, n)$. At the large scale of data, this requires an approximation by sampling, see the SI for details. The results are shown in the second and last rows of Table 1.

When the area to be super-resolved is small, we can perform epitomic LSR *using the imagery itself as an epitome*. We experiment with small tiles from **North** (256×256 up to 2048×2048 pixels). For a given tile, we initialize an epitome with the same size as the tile, with uniform prior, mean equal to the true pixel intensities, and fixed variance $\sigma^2 = 0.01$. We then embed low-res NLCD labels from the tile into this epitome just as described above and run the LSR inference algorithm. The probabilities $p(\ell|m, n)$ are then the predicted land cover labels⁶. An example appears in Fig. 6, and more in the SI. The results of this *self-epitomic* LSR, performed on a large evaluation set dissected into tiles of different sizes, can be seen in Table 1.

Results. From Table 1, we draw the following conclusions:

⁶ We found it helpful to work with $2 \times$ downsampled images and use 7×7 patches for embedding, with approximately $0.05|W|^2$ patches sampled for tiles of size $W \times W$.

*Epitomes trained only on imagery and high-res labels in **South** transfer better to **North** than U-Nets that use the same data.* The U-Nets trained only on imagery and high-res labels in the **South** region transfer poorly to **North**: patterns associated, for example, with forests in the **North** are more frequently associated with fields in **South**, and the discriminatively trained models couple the high-frequency patterns in **South** with their associated land cover labels. Most surprisingly, even the U-Nets trained on the LR **North** imagery perform worse than any of the epitome models trained on the same data.⁷

There is evidence that the far better transfer performance of the epitomes is due to generative training. First, it is nearly unsupervised: no labels are seen in training, except to weakly guide the sampling of patches. Second, diversification training ensures, for example, that forests resembling those found in **North**, while rare, still appear in the epitomes trained on **South** imagery and receive somewhat accurate label embeddings. The posterior on those areas of the epitomes is then much higher in the **North**. (In the SI we show the mean posteriors over epitome positions illustrating this point.)

The self-similarity in images that defines the repetition of patterns in certain classes is highly local. If we were to study self-similarity in a large region, we would be bound to find that some imagery patterns that are associated with a particular high-res label in one area are less so in another. Therefore, the size of the area on which to perform LSR reasoning is an important design parameter. If the area is too small, then we may not get enough observations of coarse classes to unambiguously assign high-res patterns to them: indeed, self-epitomic LSR accuracy increases with the size of the tile. It is remarkable that we can get better high-res segmentation results than the state of the art by studying one 512×512 patch at a time, together with low-res classes for 30×30 blocks, and no other training data or high-res labels.

On the other hand, when the area is too large, then the pattern diversity increases and ambiguity may reduce the effectiveness of the method. Furthermore, when the area is too large, self-epitomic LSR is not computationally practicable – the imagery must be compressed in an epitome to mine self-similarity. All-tile epitomic LSR improves over the baseline models although *no high-res labels are seen*, while the best-performing U-Nets required high-res labels in **South**, low-res classes in **North**, and imagery from both **South** and **North** in training.

5.2 Lymphocyte segmentation in pathology images

Our second example is the task of identifying tumor-infiltrating lymphocytes (TILs) in pathology imagery. We work with a set of 50000 240×240 crops of $0.5\mu\text{m}$ -resolution H&E-stained tumor imagery [39]. There is no high-res *segmentation* data available for this task. However, [18] produced a set of 1786 images centered on single cells, labeled with whether the center cell is a TIL, on which our methods can be evaluated.

⁷ We used training settings identical to those of [25]. The training collapsed to a minimum in which the “water” class was not predicted, but the accuracy would be lower than that of all-tile epitomic LSR even if all water were predicted correctly.

Table 2. Performance of various methods on the TIL segmentation task. We report the area under the ROC curve

Model	Label training set	AUC
Manual features SVM [46,18]	HR	0.713
CNN [18]	HR	0.494
CNN with pretraining [18]	HR	0.786
U-Net neural LSR [25]	LR + color masks	0.783
Non-div. epitomic LSR	LR	0.794
Div. epitomic LSR	LR	0.801

The best results for this task that used high-resolution supervision required either a manually tuned feature extraction pipeline and SVM classifier [46,18] or, in the case of CNNs, a sparse autoencoder pretraining mechanism [18]. More recently, [25] nearly matched the supervised CNN results using the neural label super-resolution technique: the only guidance available to the segmentation model in training was low-resolution estimates of the probability of TIL infiltration in 100×100 regions for the entire dataset derived by [39], as well as weak pixel-level rules (masking regions below certain thresholds of hematoxylin level).

We address the same problem as [25], using the low-res probability maps as the only supervision in epitomic LSR:

Epitome training. We train 299×299 epitomes on patches of size 11×11 to 31×31 intersecting the center pixels of the images to be segmented. The resulting models trained with and without self-diversification are shown in Fig. 7.

Low-resolution embedding. Following [25], we define 10 classes c , for each range of density estimates $[0.1 \cdot n, 0.1 \cdot (n + 1)]$. We find the posteriors $p(m, n|c)$ by embedding 1 million 11×11 patches from the entire dataset.

Epitomic label super-resolution. We estimate the mean TIL densities in each probability range, $p(\ell|c)$ and set a uniform prior $p(c)$. We then produce the probabilities of TIL presence per position $p(\ell|m, n)$ by the LSR algorithm.

We then evaluate our models on the data for which high-res labels exist by sampling 11×11 patches x containing the center pixel – 100 for each test image – and computing the mean probability of TIL presence $\sum_s p(\ell|s)p(s|x)$ as the final prediction score. We obtained better results when we instead averaged the probability of TIL presence *anywhere* in an embedded patch in the epitome, that is, convolved $p(\ell|s)$ with a 11×11 uniform filter before computing this sum.

Results. As summarized in Table 2, our epitomic LSR outperforms all previous methods, including both the supervised models and the neural LSR, with self-diversifying epitomes providing the greatest improvement. The results suggest that TIL identification is a highly local problem. Deep CNNs, with their large receptive fields, require hand-engineered features or unsupervised pretraining to reach even comparable performance. In addition, epitomes are entirely unsupervised and thus amenable to adaptation to new tasks, such as classifying other types of cells: given coarse label data, we may simply embed it into the pretrained epitomes and perform LSR.

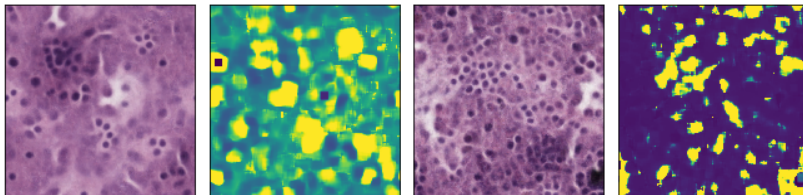


Fig. 7. Epitomes trained on tumor imagery and the embedding of the tumor-infiltrating lymphocyte label. The model on the right was trained with self-diversification

6 Conclusion

Motivated by the observation that deep convolutional networks usually have a small effective receptive field, we revisit simple patch mixture models, in particular, epitomes. As generative models that allow addition of latent variables, these approaches have several advantages. They are interpretable: an epitome looks like the imagery on which it was trained (Fig. 2), and examining the posteriors over epitome positions is akin to understanding weights for many neurons at once. The desired invariances can be directly modeled with additional hidden variables, just as [12] modeled illumination. They can be combined with other statistical procedures, as we show with our novel label super-resolution formulation (Sec. 4). They can be pretrained on a large amount of unlabeled data so that a small number of labeled points are needed to train prediction models, and they can be a base of hierarchical or pyramidal models that reason over long ranges, e.g., [9,34,43,11,23]. Using epitome-derived features in tasks that require long-range reasoning, such as common benchmarks for segmentation or classification of large images, is an interesting subject for future work.

Just as deep neural networks suffered from the vanishing gradient problem for years, before such innovations as stagewise pretraining [15], dropout [42], and the recognition of the numerical advantages of ReLU units [26], epitomic representations had suffered from their own numerical problems stemming from the large dynamic range of the posterior distributions. As a remedy, we designed a new large-scale learning algorithm that allowed us to run experiments on hundreds of billions of pixels. We showed that simply through mining patch self-similarity, epitomic representations outperform the neural state of the art in domain transfer and label super-resolution in two important application domains.

We direct the reader to the SI for more examples, code, results on another competition dataset (in which epitomes were the basis for the winning method [36]), and discussion on future research.

Acknowledgments: The authors thank Caleb Robinson for valuable help with experiments [36] and the reviewers for comments on earlier versions of the paper.

References

1. Modis/terra+aqua land cover type yearly l3 global 500m. <http://doi.org/10.5067/MODIS/mcd12q1.006>
2. 2019 ieee grss data fusion contest results. <http://www.grss-ieee.org/community/technical-committees/data-fusion/2019-ieee-grss-data-fusion-contest-results/> (2020)
3. 2020 ieee grss data fusion contest. <https://competitions.codalab.org/competitions/22289#results> (2020)
4. 2020 ieee grss data fusion contest. <http://www.grss-ieee.org/community/technical-committees/data-fusion/> (2020)
5. 2020 ieee grss data fusion contest results. <http://www.grss-ieee.org/community/technical-committees/data-fusion/2020-ieee-grss-data-fusion-contest-results/> (2020)
6. Bazzani, L., Cristani, M., Perina, A., Murino, V.: Multiple-shot person re-identification by chromatic and epitomic analyses. *Pattern Recognition Letters* **33**(7), 898–903 (2012)
7. Brendel, W., Bethge, M.: Approximating CNNs with bag-of-local-features models works surprisingly well on imagenet. In: *International Conference on Learning Representations (ICLR)* (2019)
8. Chesapeake Conservancy: Land cover data project (January 2017), <https://chesapeakeconservancy.org/wp-content/uploads/2017/01/LandCover101Guide.pdf>, [Online]
9. Cheung, V., Jojic, N., Samaras, D.: Capturing long-range correlations with patch models. In: *2007 IEEE Conference on Computer Vision and Pattern Recognition*. pp. 1–8. IEEE (2007)
10. Dai, J., He, K., Sun, J.: Boxsup: Exploiting bounding boxes to supervise convolutional networks for semantic segmentation. In: *Proceedings of the IEEE International Conference on Computer Vision*. pp. 1635–1643 (2015)
11. Fergus, R., Fei-Fei, L., Perona, P., Zisserman, A.: Learning object categories from google’s image search. In: *Tenth IEEE International Conference on Computer Vision (ICCV’05) Volume 1*. vol. 2, pp. 1816–1823. IEEE (2005)
12. Frey, B.J., Jojic, N.: Transformed component analysis: Joint estimation of spatial transformations and image components. In: *Proceedings of the Seventh IEEE International Conference on Computer Vision*. vol. 2, pp. 1190–1196. IEEE (1999)
13. Ganchev, K., Gillenwater, J., Taskar, B., et al.: Posterior regularization for structured latent variable models. *Journal of Machine Learning Research* **11**(Jul), 2001–2049 (2010)
14. Geirhos, R., Rubisch, P., Michaelis, C., Bethge, M., Wichmann, F.A., Brendel, W.: Imagenet-trained CNNs are biased towards texture; increasing shape bias improves accuracy and robustness. In: *International Conference on Learning Representations (ICLR)* (2019)
15. Hinton, G.E., Salakhutdinov, R.R.: Reducing the dimensionality of data with neural networks. *science* **313**(5786), 504–507 (2006)
16. Homer, C., Dewitz, J., Yang, L., Jin, S., Danielson, P., Xian, G., Coulston, J., Herold, N., Wickham, J., Megown, K.: Completion of the 2011 national land cover database for the conterminous united states—representing a decade of land cover change information. *Photogrammetric Engineering & Remote Sensing* **81**(5), 345–354 (2015)

17. Hong, S., Noh, H., Han, B.: Decoupled deep neural network for semi-supervised semantic segmentation. In: *Advances in neural information processing systems*. pp. 1495–1503 (2015)
18. Hou, L., Nguyen, V., Kanevsky, A.B., Samaras, D., Kurc, T.M., Zhao, T., Gupta, R.R., Gao, Y., Chen, W., Foran, D., et al.: Sparse autoencoder for unsupervised nucleus detection and representation in histopathology images. *Pattern Recognition* (2018)
19. Jojic, N., Caspi, Y.: Capturing image structure with probabilistic index maps. In: *Proceedings of the 2004 IEEE Computer Society Conference on Computer Vision and Pattern Recognition, 2004. CVPR 2004*. vol. 1, pp. I–I. IEEE (2004)
20. Jojic, N., Frey, B.J., Kannan, A.: Epitomic analysis of appearance and shape. In: *ICCV*. vol. 3, p. 34 (2003)
21. Jojic, N., Perina, A., Murino, V.: Structural epitome: a way to summarize one’s visual experience. In: *Advances in neural information processing systems*. pp. 1027–1035 (2010)
22. Kingma, D., Ba, J.: Adam: A method for stochastic optimization. *International Conference on Learning Representations* (12 2014)
23. Lazebnik, S., Schmid, C., Ponce, J.: Beyond bags of features: Spatial pyramid matching for recognizing natural scene categories. In: *2006 IEEE Computer Society Conference on Computer Vision and Pattern Recognition (CVPR’06)*. vol. 2, pp. 2169–2178. IEEE (2006)
24. Luo, W., Li, Y., Urtasun, R., Zemel, R.: Understanding the effective receptive field in deep convolutional neural networks. In: Lee, D.D., Sugiyama, M., Luxburg, U.V., Guyon, I., Garnett, R. (eds.) *Advances in Neural Information Processing Systems 29*, pp. 4898–4906. Curran Associates, Inc. (2016), <http://papers.nips.cc/paper/6203-understanding-the-effective-receptive-field-in-deep-convolutional-neural-networks.pdf>
25. Malkin, K., Robinson, C., Hou, L., Soobitsky, R., Czawlytko, J., Samaras, D., Saltz, J., Joppa, L., Jojic, N.: Label super-resolution networks. *International Conference on Learning Representations* (2019)
26. Nair, V., Hinton, G.E.: Rectified linear units improve restricted boltzmann machines. In: *Proceedings of the 27th international conference on machine learning (ICML-10)*. pp. 807–814 (2010)
27. Ni, K., Kannan, A., Criminisi, A., Winn, J.: Epitomic location recognition. *IEEE transactions on pattern analysis and machine intelligence* **31**(12), 2158–2167 (2009)
28. Nilsback, M.E., Zisserman, A.: A visual vocabulary for flower classification. In: *2006 IEEE Computer Society Conference on Computer Vision and Pattern Recognition (CVPR’06)*. vol. 2, pp. 1447–1454. IEEE (2006)
29. Papandreou, G., Chen, L.C., Murphy, K.P., Yuille, A.L.: Weakly-and semi-supervised learning of a deep convolutional network for semantic image segmentation. In: *Proceedings of the IEEE international conference on computer vision*. pp. 1742–1750 (2015)
30. Papandreou, G., Chen, L.C., Yuille, A.L.: Modeling image patches with a generic dictionary of mini-epitomes. In: *Proceedings of the IEEE Conference on Computer Vision and Pattern Recognition*. pp. 2051–2058 (2014)
31. Papandreou, G., Kokkinos, I., Savalle, P.A.: Modeling local and global deformations in deep learning: Epitomic convolution, multiple instance learning, and sliding window detection. In: *Proceedings of the IEEE Conference on Computer Vision and Pattern Recognition*. pp. 390–399 (2015)

32. Paszke, A., Gross, S., Chintala, S., Chanan, G., Yang, E., DeVito, Z., Lin, Z., Desmaison, A., Antiga, L., Lerer, A.: Automatic differentiation in PyTorch. In: NIPS Autodiff Workshop (2017)
33. Pathak, D., Krahenbuhl, P., Darrell, T.: Constrained convolutional neural networks for weakly supervised segmentation. In: Proceedings of the IEEE international conference on computer vision. pp. 1796–1804 (2015)
34. Perina, A., Jojic, N.: Spring lattice counting grids: Scene recognition using deformable positional constraints. In: European Conference on Computer Vision. pp. 837–851. Springer (2012)
35. Robinson, C., Hou, L., Malkin, K., Soobitsky, R., Czawlytko, J., Dilkina, B., Jojic, N.: Large scale high-resolution land cover mapping with multi-resolution data. In: Proceedings of the IEEE Conference on Computer Vision and Pattern Recognition. pp. 12726–12735 (2019)
36. Robinson, C., Malkin, K., Hu, L., Dilkina, B., Jojic, N.: Weakly supervised semantic segmentation in the 2020 IEEE GRSS Data Fusion Contest. Proceedings of the International Geoscience and Remote Sensing Symposium (2020)
37. Ronneberger, O., Fischer, P., Brox, T.: U-net: Convolutional networks for biomedical image segmentation. In: International Conference on Medical image computing and computer-assisted intervention. pp. 234–241. Springer (2015)
38. Russakovsky, O., Deng, J., Su, H., Krause, J., Satheesh, S., Ma, S., Huang, Z., Karpathy, A., Khosla, A., Bernstein, M., et al.: Imagenet large scale visual recognition challenge. *International journal of computer vision* **115**(3), 211–252 (2015)
39. Saltz, J., Gupta, R., Hou, L., Kurc, T., Singh, P., Nguyen, V., Samaras, D., Shroyer, K.R., Zhao, T., Batiste, R., et al.: Spatial organization and molecular correlation of tumor-infiltrating lymphocytes using deep learning on pathology images. *Cell reports* **23**(1), 181 (2018)
40. Schmitt, M., Hughes, L.H., Qiu, C., Zhu, X.X.: Sen12ms—a curated dataset of georeferenced multi-spectral sentinel-1/2 imagery for deep learning and data fusion. *ISPRS Journal of Photogrammetry and Remote Sensing* (2020)
41. Schmitt, M., Prexl, J., Ebel, P., Liebel, L., Zhu, X.X.: Weakly supervised semantic segmentation of satellite images for land cover mapping—challenges and opportunities. arXiv preprint arXiv:2002.08254 (2020)
42. Srivastava, N., Hinton, G., Krizhevsky, A., Sutskever, I., Salakhutdinov, R.: Dropout: a simple way to prevent neural networks from overfitting. *The journal of machine learning research* **15**(1), 1929–1958 (2014)
43. Weber, M., Welling, M., Perona, P.: Unsupervised learning of models for recognition. In: European conference on computer vision. pp. 18–32. Springer (2000)
44. Yeung, S., Kannan, A., Dauphin, Y., Fei-Fei, L.: Epitomic variational autoencoders (2016)
45. Zhang, H., Fritts, J.E., Goldman, S.A.: Image segmentation evaluation: A survey of unsupervised methods. *computer vision and image understanding* **110**(2), 260–280 (2008)
46. Zhou, N., Yu, X., Zhao, T., Wen, S., Wang, F., Zhu, W., Kurc, T., Tannenbaum, A., Saltz, J., Gao, Y.: Evaluation of nucleus segmentation in digital pathology images through large scale image synthesis. In: Medical Imaging 2017: Digital Pathology. vol. 10140, p. 101400K. International Society for Optics and Photonics (2017)

A Code

We provide sample code at https://github.com/anthonymlortiz/epitomes_lsr. The folder `data/` includes an example of a $2 \times$ downsampled 2×2 km tile of aerial imagery and the associated high-res and low-res labels. Run the notebook `train_epitome.ipynb` to visualize the iterations of epitome training on this area. Run `self_epitomic_sr.ipynb` to visualize single-image label super-resolution. (The corresponding static HTML files can also be used for viewing. Some outputs of the first notebook are shown in Fig. 8.)

The training code is short and clear, and we feel that it can serve in lieu of pseudocode. The reader can immediately run it, perhaps even with their own data.

B The vanishing posterior problem in EM and SGD epitome learning

As derived in [20], the original EM algorithm for epitome learning optimizes the log likelihood

$$\sum_t \log \sum_{s=1}^S p(x^t|s)p(s) \quad (12)$$

by iterating two steps. First, the image patches x^t are mapped to the epitome using the posterior $p(s|x) \propto p(x|s)p(s)$, with

$$\begin{aligned} \log p(s_1, s_2|x) = \text{const} + \sum_{i,j,k} \frac{-1}{2} \left(\frac{x_{i,j,k}^2}{\sigma_{s_1+i, s_2+j, k}^2} - \frac{2x_{i,j,k}\mu_{s_1+i, s_2+j, k}}{\sigma_{s_1+i, s_2+j, k}^2} \right. \\ \left. + \frac{\mu_{s_1+i, s_2+j, k}^2}{\sigma_{s_1+i, s_2+j, k}^2} + \log \sigma_{s_1+i, s_2+j, k}^2 \right) + \log p(s_1, s_2). \end{aligned} \quad (13)$$

Thus, the E step is efficiently performed with convolutions, creating the posterior $p(s|x)$ used in the M step which re-estimates epitome parameters by averaging the pixels from the patches based on their locations and posterior mapping. For example, the mean epitome is re-estimated as

$$\mu_{m,n,k} = \frac{\sum_t \sum_{(s_1, s_2)} x_{m-s_1, n-s_2, k}^t p(s_1, s_2|x^t)}{\sum_t \sum_{s_1, s_2} p(s_1, s_2|x^t)} \quad (14)$$

where inner summations over s_1, s_2 in numerator and denominator are performed over windows W_{s_1, s_2} containing the pixel m, n : for a $K \times K$ patch x^t , (s_1, s_2) goes from $(m - K + 1, n - K + 1)$ to (m, n) . We readily recognize that both numerator and denominator consist of convolutions of the $K \times K$ patch x^t with the posterior $N \times N$ posterior map $p(s_1, s_2|x^t)$ over an $N \times N$ epitome.

The main numerical difficulty with epitome training is that the posterior map can be zero in many places, as the consequence of a large dynamic range of the

values computed in Eq. 5, especially as the variances contract during learning. Upon exponentiation to obtain $p(s|x)$, some locations in the epitome may get their probability clipped to zero. If all data patches avoid certain pixels in the epitome, then those locations stop being updated. Note that this is not a local minimum problem, but purely a numerical precision issue. Avoiding division by zero by adding a small constant to the numerator and the denominator in Eq. 14 and subtracting the maximum in Eq. 5 before exponentiation do nothing to remedy this problem: The areas of the epitome that die off simply get filled with the mean of all pixels seen in training. In practice EM training usually has to be carefully coaxed out of these situations, for example by training first with larger patches and later with smaller ones. The larger patches hit more pixels, making it less likely that some epitome locations will never be part of the component s for which at least one data point x^t shows a measurable posterior after exponentiation. For a regular mixture model the problem can be remedied by keeping track of the highest value of the posterior $p(s|x^t)$ over all data points. In epitomes, because of parameter sharing, this is not trivial. In [21], the authors introduce a solution which evaluates different epitome parts with different levels of precision. The number of precision levels is finite, and the complexity of the learning algorithm scales linearly with the number of levels, which makes the approach impractical for very large epitomes where we could have very large dynamic ranges in the posterior.

The numerical difficulties arising from vanishing posteriors persist if the model is trained by stochastic gradient descent on the parameters of the model. For a mixture model $p(x) = \sum_s p(x|s)p(s)$, with the mixture components $p(x|s) = p(x; \theta_s)$ and the prior $p(s) \propto e^{\pi_s}$, the posterior factors into the gradient of the log-likelihood:

$$\begin{aligned} \frac{d \log p(x; \theta, \pi)}{d\theta_{s_1, s_2}} &= p(s_1, s_2|x; \theta, \pi) \frac{d \log p(x; \theta)}{d\theta_{s_1, s_2}}, \\ \frac{d \log p(x; \theta, \pi)}{d\pi_{s_1, s_2}} &= p(s_1, s_2|x; \theta, \pi). \end{aligned}$$

In the situation of epitomes, some θ_s are shared among different s . The gradients with respect to parameters at a given position vanish if all posteriors in a window around the position vanish. Furthermore, batch training and the posterior sampling described below can make it even more likely to lose parts of the epitome during training. As described in Section 3 of the main text, we use a location promotion strategy to solve this problem.

C Large scale epitome training details

C.1 Training details and parameters

All of our epitome models were implemented using the PyTorch package [32] for efficient computation on the GPU; we also have efficient Matlab implementations for CPU. The epitomes are trained on variable-size patches, 11×11 to $31 \times$

31. For patches of size w , we smooth the probabilities $p(x^t|s)$ by temperature $(w/11)^2$. The means are initialized randomly, distributed as $0.5 + \text{unif}(0, 0.1)$. For stability, the variances are parametrized by their inverses $1/\sigma^2$, initialized at 10 and clipped between 1 and 100, and the priors are parametrized in the log domain, initialized at 0 and clipped between -4 and 4. They were trained for 50000 iterations with a batch size of 256 (aerial imagery) or 30000 iterations with a batch size of 64 (pathology imagery), using the Adam optimizer [22] with initial learning rate 0.003.

For the location promotion mechanism in training, we use a threshold of $10^{-8} \cdot (\text{batch size})$. For the 499×499 aerial imagery epitomes, this amounts to $c \approx 0.64$, and for the 299×299 pathology epitomes, $c \approx 0.057$. The counter reset threshold is $\delta = 0.05$: after 0.95 of the epitome has hit its threshold, the counters are zeroed.

C.2 Evaluation by sampling

Here we explain the high-res label embedding and reconstruction method mentioned in Section 5.1. For a given patch x with high-res labels y , we compute the posterior distribution of epitome positions $p(s|x)$. To embed the labels y – that is, to add them, appropriately weighted, to the counts that give $p(\ell|m, n)$, it would be necessary to convolve the 11×11 patch of *labels* with the posterior. It is more efficient, and equivalent in expectation, to sample several locations from the posterior distribution and to add the labels y to the counts surrounding those locations. We use 16 samples in our experiments. (Because the posterior distributions tend to be peaky, this does not affect the results greatly.) This also explains why there are unmapped areas in the middle column of Fig. 5: the eight epitomes were trained individually, but when they were combined as components of a uniform mixture, those areas were captured by the other epitomes and were never sampled. Similarly, in reconstruction, for a given patch x , we sample several positions s_n^* from the posterior distribution and sum the labels in windows around the s_n^* to form the output predictions for x .

C.3 Execution time

In this section we report the execution times for both U-Nets and epitome algorithms used in our land cover experiments. The EM algorithm for label super-resolution, which consists of iterative matrix multiplications and normalizations, runs in not more than a few seconds, and the main computational cost is incurred in training and evaluation.

The training of one set of four land cover epitomes and of a U-Net both take about 12 hours in our implementation. Note that the two models were implemented in different neural net toolkits: the U-Net implementation in the CNTK toolkit by the authors of [25,35] is two years old and ran on a different version of the CUDA library than our implementation of epitomes in Torch.

The average evaluation times per pixel with different methods are reported in Table 3. For the epitomes, the execution time does not include the label

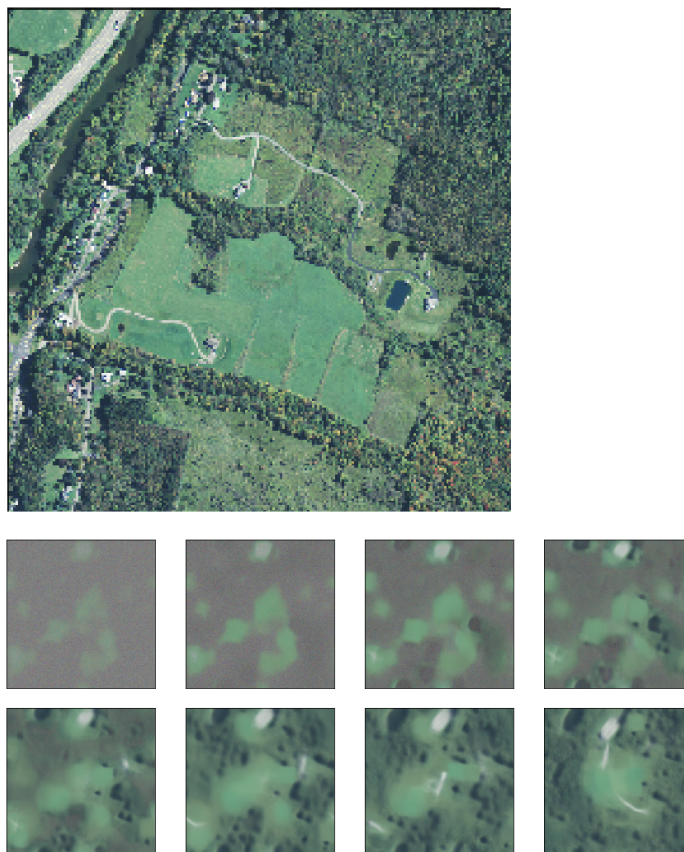


Fig. 8. The 1024×1024 image from our sample code (*above*) and 299×299 epitome μ parameters at selected iterations of epitome training (after 32, 64, 128, \dots , 4096 batches of 256 patches), shown at the same scale (*below*)

embedding (which can be done incrementally at training time) or the (fast) label super-resolution inference algorithm. On the other hand, for the self-epitomic LSR results, we sampled 5% of all 7×7 patches in the input tile for the low-resolution label embedding; this computation forms the bulk of the computation time, since the LSR algorithm immediately produces the target high-resolution labels without the need to reevaluate the posterior mappings.

We see a number of optimizations to the epitome algorithms that are likely to speed up the evaluation. For example, some terms in the expression for the posterior are independent of the input patch and can be precomputed. In addition, our epitome code does not use the optimized multithreaded data loading methods that appear in the U-Net implementation.

Table 3. Execution times (per pixel) of various algorithms on the land cover data.

Method	parameters	time / thousand pixels
U-Net	256×256 input	3ms
All-tile epitomic LSR	11×11 windows, one sample	53ms
All-tile epitomic LSR	31×31 windows, one sample	29ms
Self-epitomic LSR	128×128 input	7ms
Self-epitomic LSR	256×256 input	8ms
Self-epitomic LSR	512×512 input	25ms
Self-epitomic LSR	1024×1024 input	94ms

D On domain transfer: Comparison of the posterior distributions for land cover regions

Fig. 9 shows the eight components of the land cover epitome (Fig. 5 in the main text) and the posterior distributions in the **South** and **North** regions. Observe that the **South** data is more uniformly mapped. Also, notice the different distribution in forested areas: for example, the light-green forests are rare in **North**. The change in data distribution is in this way easily detectable and explain why U-Nets do not transfer from the **South** to the **North**. Our epitome training is based on the diversification criterion targeting only the distribution over the input patches x^t , but favoring the worst modeled patches. The forests of the **North** where U-Nets make errors can actually be found in the South, too, but they are just more rare. The diversification training learns these patterns, too, and the epitomic classification is not confused by these patterns in the North, resulting in 20% increase in accuracy (see the top of Table 1 in the main text).

E Label super-resolution

In Fig. 12 we provide the standard National Land Cover Database (NLCD) class descriptions [16] and color legend in Fig. 12. We use the same colors in all NLCD

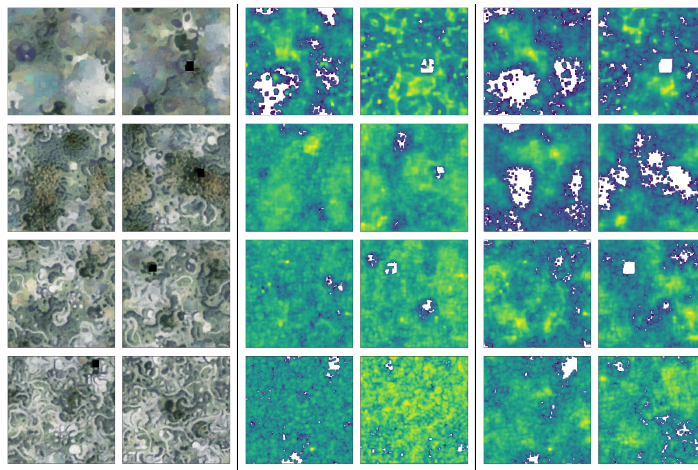


Fig. 9. Epitomes (total area $2 \cdot 10^6$ pixels) trained on imagery from the **South** region (*left*), the log posterior over positions for 31×31 patches in the **South** region (*middle*), the log posterior over positions for 31×31 patches in the **North** region (*right*)

visualizations here and in the main text. In Table 4 we also provide the $p(\ell|c)$ statistics from [25] which we used in our experiments.

In Fig. 11 we show a few more results of the single-tile LSR technique for visual inspection of both accurate and inaccurate predictions. But first, as promised in the main text, we address the possibility of performing LSR simply using pixel colors.

As discussed in the main text, our label super-resolution technique iterates equations

$$q_{\ell,c}(s) \propto p(\ell|s)p(s|c). \quad (15)$$

and

$$p(\ell|s) \propto \sum_c p(c)p(\ell|c)q_{\ell,c}(s). \quad (16)$$

Here, we assume that the texture components indexed by s are associated with classes c through $p(s|c)$, and the iterative procedure finds association between the components and high-res labels ℓ , i.e. the distribution $p(\ell|s)$. A straightforward interpretation of this is that components s are associated with image patches, and so $p(\ell|s)$ only tells us the (probability of) label ℓ of the whole prototype s , and therefore the patches mapped to it. Thus, without the epitomic reasoning in Eq. 8 in the main text, the granularity with which we can assign high-res labels would depend on the patch size, and to get to the highest possible resolution, we would have to assume that s indexes the prototypes of a *single* pixel size. In other words, s would simply refer to a color clustering of the image (precisely, a component of a mixture model on colors).

Fig. 10 illustrates such an approach. Using a single 1km^2 RGBI tile, we train a mixture of 48 4-dimensional diagonal Gaussians indexed by s and show the



Fig. 10. Color LSR

cluster assignments for each pixel to these 48 clusters using a random color palette. The term $p(s|c)$ is then computed simply by computing the 48×20 matrix of co-occurrences of clusters s and coarse classes c , which are also shown in the figure, and then normalizing the matrix appropriately. Iterating the two equations above now leads to the 4×48 mapping of labels ℓ to components s in form of the distribution $p(\ell|s)$. When the most likely label is assigned to each cluster, we obtain the LSR result shown in the last panel in the figure. The resulting HR predictions are remarkable given that only pixel colors were used, but they also, unsurprisingly, exhibit a scattering of predicted impervious pixels all over the image, and in general a fairly speckled result. In addition, the model confuses the main road in the patch with fields and forests. On the other hand, the epitomic pixel-wise reasoning described in the main text yields the result shown in the first row of Fig. 11, where the road is accurately predicted and the speckles are generally suppressed, indicating that our technique reasons about larger patterns and the individual pixels within them to assign single-pixel-level labels.

F Epitomic LSR in the 2020 IEEE-GRSS Data Fusion Contest

The IEEE Geoscience and Remote Sensing Society ran a competition on a task almost identical to the label super-resolution application on land cover described in the main paper. We show here that we can reach the top result in the competition through analysis *only* of the validation set (986 images), without ever looking at the very large training set of over 180k pairs of satellite images and their low-res labels. A detailed description of the winning method can be found in [36].

The goal of the 2020 IEEE GRSS data fusion competition [3] was to infer high-resolution (10m) labels in 8 classes (forest, shrubland, grassland, wetland, cropland, urban, barren, water) based on high-resolution (10m) 12-band Sentinel imagery and low-resolution (500m) MODIS labels (Fig. 14). To that end, a training set of around 180k 256×256 Sentinel images [40] and the corresponding MODIS labels [1] was provided, and the competition was performed on class average accuracy on a validation set (986 images) and a test set. We examine the validation set stage of the competition, in which 70 teams officially participated.

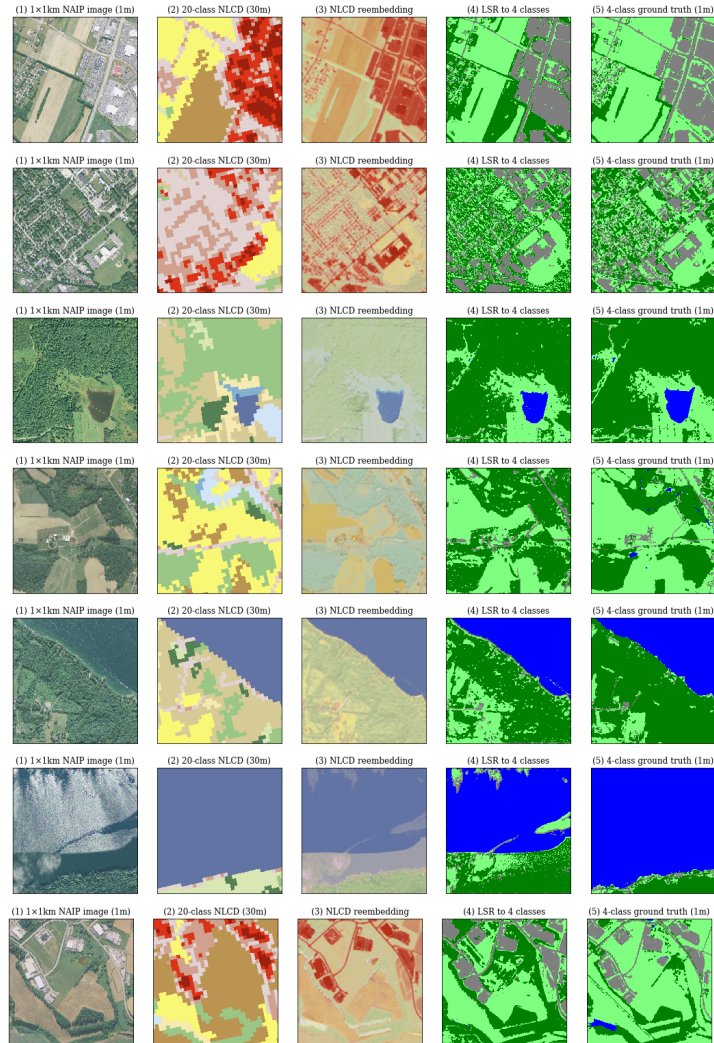


Fig. 11. Examples of single-tile (self-epitomic) LSR using 7×7 patches on $2 \times$ downsampled images. The first row provides the analysis of the same tile shown super-resolved with a simple color model in Fig. 10. The rest are selected to illustrate both the success and failure modes of the single-tile approach

Class Value	Classification Description
Water	
11	Open Water - areas of open water, generally with less than 25% cover of vegetation or soil.
12	Perennial Ice/Snow - areas characterized by a perennial cover of ice and/or snow, generally greater than 25% of total cover.
Developed	
21	Developed, Open Space - areas with a mixture of some constructed materials, but mostly vegetation in the form of lawn grasses. Impervious surfaces account for less than 20% of total cover. These areas most commonly include large-lot single-family housing units, parks, golf courses, and vegetation planted in developed settings for recreation, erosion control, or aesthetic purposes.
22	Developed, Low Intensity - areas with a mixture of constructed materials and vegetation. Impervious surfaces account for 20% to 49% percent of total cover. These areas most commonly include single-family housing units.
23	Developed, Medium Intensity - areas with a mixture of constructed materials and vegetation. Impervious surfaces account for 50% to 79% of the total cover. These areas most commonly include single-family housing units.
24	Developed High Intensity - highly developed areas where people (buildings or work in that number). Examples include apartment complexes, row houses, and commercial/industrial. Impervious surfaces account for 80% to 100% of the total cover.
Barren	
31	Barren Land (Rock/Sand/Clay) - areas of bedrock, desert pavement, scarp, talus, slides, volcanic material, glacial debris, sand dunes, strip mines, gravel pits and other accumulations of earthen material. Generally, vegetation accounts for less than 15% of total cover.
Forest	
41	Deciduous Forest - areas dominated by trees generally greater than 5 meters tall, and greater than 20% of total vegetation cover. More than 75% of the tree species shed foliage simultaneously in response to seasonal change.
42	Evergreen Forest - areas dominated by trees generally greater than 5 meters tall, and greater than 20% of total vegetation cover. More than 75% of the tree species maintain their leaves all year. Canopy is never without green foliage.
43	Mixed Forest - areas dominated by trees generally greater than 5 meters tall, and greater than 20% of total vegetation cover. Neither deciduous nor evergreen species are greater than 75% of total tree cover.
Shrubland	
51	Dwarf Scrub - Alaska only areas dominated by shrubs less than 20 centimeters tall with shrub canopy typically greater than 20% of total vegetation. This type is often co-associated with grasses, sedges, herbs, and non-vascular vegetation.
52	Shrub/Scrub - areas dominated by shrubs; less than 5 meters tall with shrub canopy typically greater than 20% of total vegetation. This class includes true shrubs, young trees in an early successional stage or trees stunted from environmental conditions.
Herbaceous	
71	Grassland/Herbaceous - areas dominated by graminoid or herbaceous vegetation, generally greater than 80% of total vegetation. These areas are not subject to intensive management such as tilling, but can be utilized for grazing.
72	Sedge/Herbaceous - Alaska only areas dominated by sedges and forbs, generally greater than 80% of total vegetation. This type can occur with significant other grasses or other grass like plants, and includes sedge tundra, and sedge tussock tundra.
73	Lichens - Alaska only areas dominated by fruticose or foliose lichens generally greater than 80% of total vegetation.
74	Moss - Alaska only areas dominated by mosses, generally greater than 80% of total vegetation.
Planted/Cultivated	
81	Pasture/Hay - areas of grasses, legumes, or grass-legume mixtures planted for livestock grazing or the production of seed or hay crops, typically on a perennial cycle. Pasture/hay vegetation accounts for greater than 20% of total vegetation.
82	Cultivated Crops - areas used for the production of annual crops, such as corn, soybeans, vegetables, tobacco, and cotton, and also perennial woody crops such as orchards and vineyards. Crop vegetation accounts for greater than 20% of total vegetation. This class also includes all land being actively tilled.
Wetlands	
90	Woody Wetlands - areas where forest or shrubland vegetation accounts for greater than 20% of vegetative cover and the soil or substrate is periodically saturated with or covered with water.
95	Emergent Herbaceous Wetlands - Areas where perennial herbaceous vegetation accounts for greater than 80% of vegetative cover and the soil or substrate is periodically saturated with or covered with water.

Fig. 12. National land cover database (NLCD) legend: descriptions and the color code [16]

Table 4. Statistics $p(\ell|c)$ of the four HR labels in 15 of the 20 land cover classes that appear in our data. Statistics are from [25]. Our model did not use the available uncertainty in the statistics, but priors can easily be added in our model (see the future work section)

NLCD class	water	forest	field	imperv.
Open water	.97	.01	.01	.02
Developed, Open Space	.00	.42	.46	.11
Developed, Low	.01	.31	.34	.35
Developed, Medium	.01	.14	.21	.63
Developed, High	.01	.03	.07	.89
Barren Land	.09	.13	.45	.32
Deciduous Forest	.00	.92	.06	.01
Evergreen Forest	.00	.94	.05	.01
Mixed Forest	.01	.92	.06	.02
Shrub/Scrub	.00	.71	.26	.03
Grassland/Herbaceous	.01	.38	.54	.07
Pasture/Hay	.00	.11	.86	.03
Cultivated Crops	.00	.11	.86	.03
Woody Wetlands	.01	.90	.08	.00
Emergent Wetlands	.11	.07	.81	.01

The ground truth high-resolution labels for the validation set have since been made publicly available [4], making the following analysis possible.

The baseline methods [41] used both random forests and deep CNNs, which all achieved average accuracy not more than 54.1%. The top 10 teams’ average accuracies on the validation set ranged between 68% and 71%. While we do not know how much data these teams used and which methods were tested by the teams in the competition, given the number of participants, it is probably safe to assume that convolutional neural networks and random forests were used in a variety of ways, as they were by the other winning teams in both this [5] and last year’s [2] contests. Yet, our approach is a straightforward mixture model as described here and in the main text.

In particular, we start with a simple color clustering model similar to the one in Sec. 4, equivalent to learning an epitome with patch size 1×1 , because Sentinel imagery has many more bands than NAIP imagery, making separation of certain classes easier. For example, richer spectral information simplifies separating water from urban/built surfaces, as well as both of those from vegetation⁸. However, classifying the rest of the classes (forests, grassland, shrubland, barren, and croplands) requires analyzing spatial patterns, so we built an 299×299 epitome model with 7×7 patches (Fig. 13). LSR is performed in each model, using as $p(\ell|c)$ the statistical table provided by Fig. 3 in [41]. Then, we ensemble these predictions.

⁸ This color clustering algorithm is augmented with a *bag of clusters* latent variable that makes the model sensitive to nearby colors. That approach is mostly independent of this work, so we direct the reader to [36] for the details.

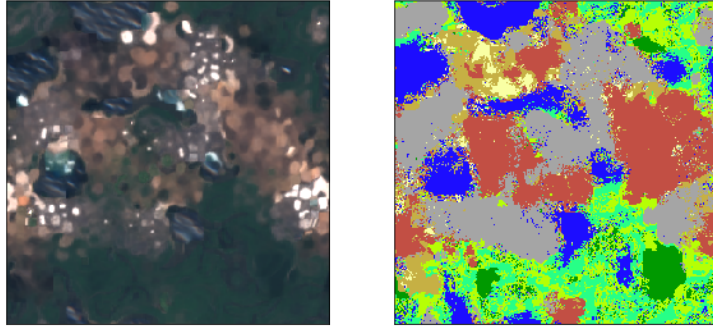


Fig. 13. 299×299 epitome of Sentinel imagery (RGB channels shown) and the output of the LSR algorithm, coded using the standard 10-class color scheme from [41]

The color-only model (1×1 patches) achieves an average accuracy of 65.4%. The epitome model (7×7 patches) yields 65.5%. Either score would rank as 14/70. We ensemble these by trusting the color-only model’s predictions on the easily confused *shrubland* and *barren* classes to get average accuracy 68%, placing the model at 11/70.

However, it is important to note that the ground truth labels themselves are not entirely accurate, as they were created in a semi-manual manner, rather than fully manually [41]. The artifacts in the ground truth labels (Fig. 14) suggest that this ‘ground truth’ is actually based on a convolutional network’s predictions (probably on lots of HR data).

To verify this, we trained a small neural network (a 5-layer fully convolutional network with two 3×3 convolutions and three 1×1 convolutions) on the predictions of our best ensemble model to introduce similar inductive biases, and this network reaches 70.7%, the top score on the leaderboard. Similar models, applied to the test set, also reached the highest accuracy of 57.5% in the main competition track.

In summary, using the simple statistical models described in this paper, it is possible to match the top score in an international competition in weakly supervised land cover mapping. Furthermore, our unsupervised learning approach is much more data-efficient than most modern-day supervised learning techniques, as evidenced by the fact that our results needed only 986 out of over 180k images in training.

G Future work

We and other researchers interested in the epitomic representations discussed here have many possible follow-up research directions to explore.

As our models are easy to interpret, they can be used in scenarios where the predictions or just their errors have to be explained. The errors of the model as

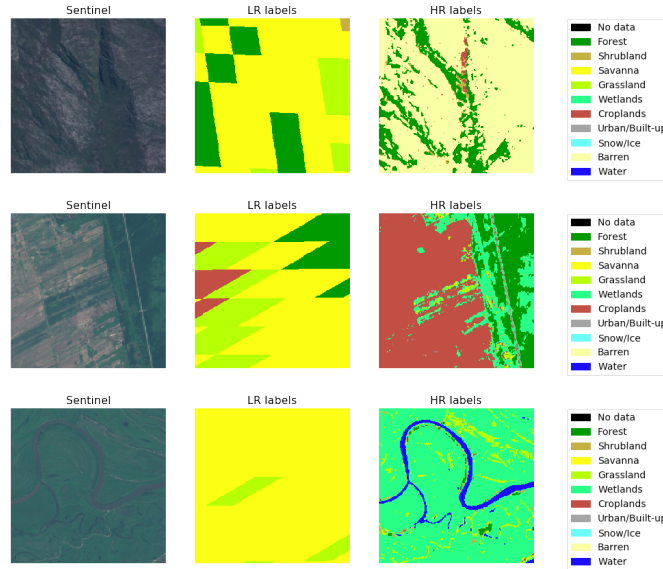


Fig. 14. Examples of high-res imagery, low-res labels, and high-res labels from the IEEE GRSS competition dataset

a predictor of high-res labels can be tracked not only to individual patches in the epitome, but through the epitome back to other patches in the data. In fact, as we discussed above, the visualization in Fig. 9 can be used to understand the domain shift of other models, such as U-Nets.

Traceability back to the training patches can also be used to further improve models through efficient hierarchical matching where the input patch is ultimately compared with an individual training patch, rather than its compressed version in the epitome.

It is also interesting to think about encoding various types of invariances as latent variables in the model, e.g. global illumination or local deformation variables.

The results in Fig. 11 all use the same statistics in Table 4 in inference, even though, clearly, the actual statistics of occurrence of different land cover labels in different NLCD classes will vary from image to image, indicating that the model is fairly robust to errors in these statistics. It would be interesting to see just how robust the approach is, and in particular, if the simplified summary statistics described in Fig. 12 could be used, or if it is possible to super-resolve a user’s estimate of label percentage in a user-defined area in human-in-the-loop schemes.

While our label super-resolution formulation only uses the average frequencies of labels ℓ in different classes c shown in Table 4 and applies these on the entire dataset, or an entire single tile, the recent LSR work [25] also used the

uncertainty estimates (variances on the frequencies across different 30m blocks). In their approach, a training cost is defined so that it uses both means and variances to match the statistics over predicted HR labels in each block, rather than summarily across the entire image. It is possible to use this information in our method, too. E.g., the label frequency variance can be used to set an appropriate Dirichlet prior on the $p(\ell|c)$ for each tile or even an individual 30m block, and then treat the parameters $p(\ell|c)$ as latent.

To infer labels for an image using the epitomes and $p(\ell|s)$ maps in Fig. 5 of the main text, we need to sample a large number of patches, covering the entire image, and compare them with the epitomes. In our current implementation, the inference time is within an order of magnitude of the U-Net’s computational cost. However, the inference can be sped up through experimentation with sampling strategies. It would also be interesting to study approximate, e.g., coarse-to-fine, epitome mapping techniques, or even learnable indexing techniques that would speed up the label inference.

It would be interesting to test epitomic representations on recognition tasks.

Previous work on epitomic representations recognized that patch models are powerful in modeling local patterns larger than the patch size, as the patches effectively get quilted into larger patterns, and just a few longer range relationships can go a long way towards grounding the quilting or capturing relationships useful in recognition [9,34]. Through a similar type of reasoning in models based on large scale epitomes it may be possible to further improve segmentation and recognition performance, e.g., in case of long features such as rivers and roads.

Recent work such as [7] has shown that the current state of the art in recognition is highly dependent on texture features, rather than image shapes. But, models we describe here can also be built on mask (shape) patches, as was shown in the paper that introduced epitomes [20], and also used in early co-segmentation work [19].

Beyond inspiration from those epitome works, we can use a variety of generative modeling work (before GANs and autoencoders), as discussed in the conclusions of the main paper, to build hierarchical models. But, using neural models of texture in combination with statistical reasoning is also possible.